

Emissivity and Optical Properties of Thin-Film Metallic Glass in the Thermal Infrared Region

Chia-Chien Lai, Tzu-Chieh Hsiao, Wei-Han Wang, Sih-Wei Chang, and Hsuen-Li Chen*

This study displays the emissivities and optical properties of thin-film metallic glasses in the thermal infrared (IR) region. It is found that the amorphous structure of the metallic glass hinders the movement of electrons, leading to unique optical properties in the thermal IR region. Measurements of the optical constants of NiNb thin-film metallic glasses reveal that a high processing pressure and sputtering power yield high optical conductivity and a low damping constant. Adjusting the parameters of the sputtering processes allows the fabrication of thin-film metallic glasses with a range of damping constants and also the change in the reflectance and emissivity. Applying optical thin film theory, the emissivity of thin-film metallic glass in the thermal IR region can be modulated. The measured emissivity of the thin-film metallic glass (45.35%) is significantly enhanced when compared with that of a Si substrate or metal film. Furthermore, the cooling ability of the optimal metallic glass is much higher than that of Si and metal films. These findings reveal that metallic glass films can display thermal radiative properties superior to those of metals and semiconductors, making them promising materials for use in electronic devices with excellent mechanical characteristics and heat dissipation properties.

and Cr₅₀Co₂₉Nb₇B₁₄ bulk metallic glasses in hydrochloric acid. These metallic glasses, with high chromium content, developed a dense passivation layer on their surfaces.^[3,4] Accordingly, metallic glasses show promising potential for diverse applications in biomedicine, the semiconductor industry, and microelectromechanical systems (MEMS).^[5] In addition, metallic glasses can assist in the fabrication of porous metals, displaying good electrical and thermal conductivities. For example, J. Yu et al. prepared nano-porous palladium through the electrochemical dealloying of Pd₃₀Ni₅₀P₂₀ metallic glass.^[6]

Developing thin-film metallic glasses has recently become a topic of investigation.^[7–10] Yiu et al. found that thin-film metallic glass can weaken the brittleness of bulk metallic glass while maintaining its excellent mechanical strength. For example, Cr₅₀Co₂₉Nb₇B₁₄ thin-film metallic glass possessed low surface energy, high strength, and, due to

its high content of chromium and the presence of niobium, excellent corrosion resistance.^[11] Moreover, thin-film metallic glass can be coated on various substrates for surface modification of the underlying materials. It can also be applied in various fields. For example, Stefanov et al. found that Al-Ni-Y and Zr-based metallic glasses have elastic limits and corrosion resistances superior to those of crystalline metal alloys. Furthermore, the average reflectance of Al-Ni-Y-Zr metallic glasses in the wavelength region from 250 to 2000 nm is ≈70%, making them possible replacement materials for the mirrors in astronomical telescopes.^[12] Moreover, Lu et al. fabricated wafer-scale metallic nanotube arrays for the detection of crystal violet through surface-enhance Raman spectroscopy (SERS).^[13] Yeh et al. used Zr₆₀Cu₂₄Al₁₁Ni₅ metallic glass to prepare reproducible and biocompatible SERS substrates.^[14]

Most previous studies of the optical properties of metallic glass have been made in the visible region. Yang et al. utilized the magnetron sputtering technique to fabricate ZrCuFeAlAg thin-film metallic glasses (TFMGs). By altering the nitrogen-doping content and adjusting the thickness of the TFMGs, they achieved a diverse color palette ranging from yellow to aqua to pink to purple.^[15] Yao et al. studied Ni₆₀Nb₄₀ thin-film metallic glass while gradually heating the substrate to a temperature close to the glass transition temperature (T_g); they found that increasing the temperature during the sputtering process gave a smoother

1. Introduction

Recent research into metallic glasses has focused mainly on their mechanical and chemical properties. The disordered structures within metallic glasses can make atomic slipping more difficult, such that they do not deform as readily as crystal metals and display excellent mechanical properties.^[1,2] Because the internal atoms of metallic glass are disordered, the corrosion resistance is also better than that of metals. Metallic glass has no crystal defects, so it can rapidly generate a uniform passivation layer on its surface to achieve good corrosion resistance. Si et al. investigated the corrosion behavior of Cr₄₀Co₃₉Nb₇B₁₄

C.-C. Lai, T.-C. Hsiao, W.-H. Wang, S.-W. Chang, H.-L. Chen
Department of Materials Science and Engineering
National Taiwan University
Taipei 10617, Taiwan
E-mail: hsuenlichen@ntu.edu.tw

H.-L. Chen
Center of Atomic Initiative for New Materials
National Taiwan University
Taipei 10617, Taiwan

 The ORCID identification number(s) for the author(s) of this article can be found under <https://doi.org/10.1002/adom.202301517>

DOI: 10.1002/adom.202301517

sample surface while also enhancing the plastic deformation stability, thermal stability, and reflectivity in the visible region.^[16] Hao et al. prepared a metallic glass-based broadband optical absorber; from an investigation of the optical properties of amorphous Au₅₅Cu₂₅Si₂₀, they achieved an average absorption of ≈95% for wavelengths in the region between 500 and 1500 nm.^[17] Moreover, in the study of the optical properties of metallic glass, Tarigan et al. used the Drude model to fit the refractive index and extinction coefficient in the wavelength range from 250 to 2500 nm of a smooth-surface sample of bulk Pt_{57.5}Cu_{14.7}Ni_{5.3}P_{22.5} metallic glass.^[18] The internal lattice-free structure of metallic glass implies that the arrangement of its atoms is in a chaotic state, causing the electrons to collide more frequently when they move in metallic glass films. Electromagnetic waves can cause the free electrons within the metal to vibrate and reflect waves with the same amplitude but with opposite phases, such that the reflection of the metal is high.^[19] Electromagnetic waves propagating in a metallic glass would be significantly different from those in a crystalline metal. To the best of our knowledge, no previous reports have described the optical properties and thermal emissivity of thin-film metallic glasses in the thermal IR region.

It is widely realized that X-ray diffraction (XRD) is capable of determining the periodic atomic structure of metallic glasses. However, the limitation of XRD is primarily related to the crystalline phase on a nanometer scale.^[20] In order to solve this problem, the transmission electron microscope (TEM) is the main instrument used to detect nanocrystals in the local area.^[21] However, preparing a TEM sample is complex, and it is also a destructive detection method. With the goal of developing a rapid and non-destructive tool for identifying the degrees of crystallinity of metallic glass films, we began by investigating the optical properties of metallic glass in the thermal IR region.

The number of transistors in integrated circuits (IC) continues to increase annually, improving the efficiency of electronic devices. With the enhanced computing power of chips, such electronic devices will generate large amounts of heat that could degrade their performance and lifetime. Effectively dissipating heat from chips will be a critical challenge for next-generation electronic devices.^[22–24] The heat dissipation of electronic devices and systems relies mainly on conduction and convection routes. Metals of high thermal conductivity have been designed with specific structures (e.g., hydrofoil-based pin fins^[25] or triangular fins^[26]) to increase the thermal conduction, convection, and heat dissipation efficiency. As the sizes of electronic devices gradually shrink and the structures of chips lead toward the third dimension, conduction- and convection-based heat dissipation methods will become more complicated, such that heat dissipation through thermal radiation might become more likely.^[27] Materials or structures with high emissivity in the thermal IR region are superior for heat dissipation through thermal radiation. Although metals are good candidates for heat dissipation through thermal conduction, their emissivity in the thermal IR region is extremely low due to the motion of the free electrons when they interact with the electric field. The surfaces of metals feature many free electrons that can move and cancel the electric field at the metal surface; therefore, the electromagnetic waves of thermal radiation cannot be emitted efficiently from metal surfaces.^[28]

Because of their disordered and amorphous structures, thin-film metallic glasses have mechanical properties and thermal emissivity properties superior to those of metals. When the atomic arrangement within a material is chaotic, the transport of electrons to and from a surface is hindered. In this study, we found that the damping constant is critical in changing the optical properties of thin-film metallic glasses. The distinct optical properties of metallic glasses in the thermal IR region can lead to higher degrees of thermal radiation than those in metals, thereby improving the heat dissipation capability of the substrates. Therefore, we applied the Drude–Lorentz model to examine the influence that disordered atomic structures have on the optical parameters. Furthermore, we found a correlation between the processing conditions and the optical properties, allowing us to improve the emissivity of metallic glass in the thermal IR region. We expect a future expansion of the applications of metallic glasses in the field of thermal management of devices and systems.

2. Results and Discussion

2.1. Thermal Emissivity Properties of NiNb Metallic Glass Film

All objects with temperatures above absolute zero emit thermal radiation. According to Kirchhoff's law, thermal emissivity (ϵ) can be described as follows:

$$\epsilon(\lambda, \theta, T) = 1 - R(\lambda, \theta, T) \quad (1)$$

where θ is the angle of incidence of the IR light and λ is its wavelength. Metals always display high reflectance (R) in the IR region because the free electrons of the metal oscillate with the incident IR wave and re-emit the energy back. As a result, the emissivity would be extremely low for crystalline metals, as demonstrated in **Figure 1a**. On the other hand, the amorphous structure of metallic glass hinders the movement of free electrons, increasing the opportunity for collision between the electrons and atoms and, thereby, increasing the absorption of the metallic glass (**Figure 1b**). Therefore, the emissivity of metallic glass is higher than that of crystal metals.

2.2. Lorentz–Drude Parameters and Optical Conductivity of NiNb Metallic Glass

To investigate the optical properties of metallic glass, we examined Ni₅₀Nb₅₀ metallic glass at wavelengths in the vis–IR range. We used the Lorentz–Drude model to fit its optical constants. The Lorentz–Drude model is a model of electron conduction that describes the dielectric and electrical properties of materials; it is based on the following equation:

$$\begin{aligned} \epsilon_r(\omega) &= 1 - \frac{\omega_p^2}{(\omega^2 + i\gamma\omega)} + \sum_{j=1}^N \frac{\omega_p^2 f_j}{(\omega_0^2 - \omega^2 - i\gamma\omega)} \\ &= 1 - \frac{\omega_p^2}{\omega^2 + \gamma^2} + i \frac{\omega_p^2 \gamma}{\omega(\omega^2 + \gamma^2)} \end{aligned} \quad (2)$$

where ω_p is the plasma frequency; γ is the damping constant; f_j is the oscillator strength; ω_0 is the resonance frequency of the

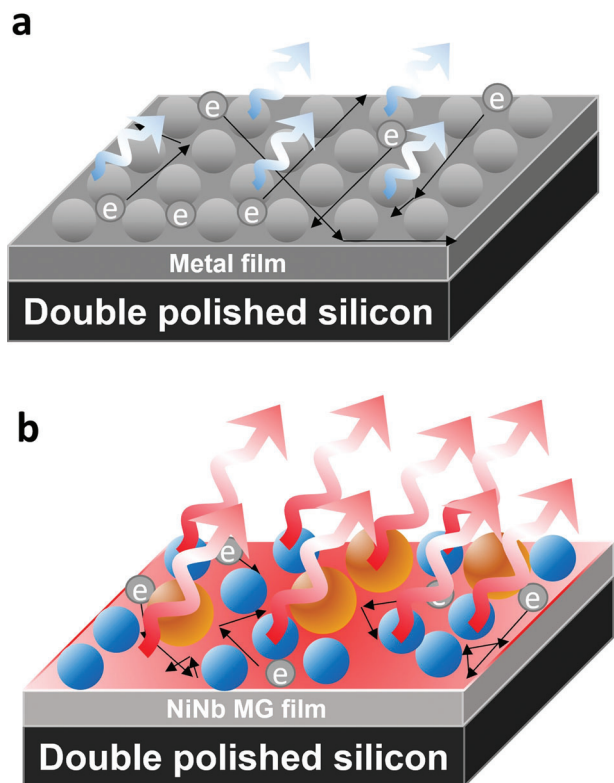


Figure 1. Schematic representation of thermal radiation and electron movement in a) a NiNb crystal metal alloy and b) a NiNb thin-film metallic glass.

oscillator; and ω is the angular frequency. The plasma frequency is the frequency above which the real part of the dielectric function becomes positive, where the metal starts to behave like a dielectric. It is proportional to the square root of the number of free electrons, as given by Equation (3):

$$\omega_p = \sqrt{\frac{Ne^2}{m\epsilon_0}} \quad (3)$$

where N is the charge carrier density, e is the charge of the electron, m is the effective mass of the material, and ϵ_0 is the permittivity in a vacuum.

The damping constant describes how often electrons in a material collide with one another. In this study, we found that the damping constant of the metallic glass was much larger than that of the metal. Because metallic glass is an amorphous material, there is no lattice inside the material within which electrons can move freely, thereby decreasing the mean free path of the electrons. Accordingly, the electron mobility will decrease in the metallic glass. **Figure 2a,b** presents the fitted refractive indices (n) and extinction coefficient (k), respectively, of Ni₅₀-Nb₅₀ metallic glass samples in the IR region. The optical constants of the Ni₅₀-Nb₅₀ metallic glasses varied depending on the deposition conditions. **Table 1** lists the processing parameters of the samples.

The optical spectra of the samples recorded with wavelengths in the region from 250 nm to 20 μm are provided in Figures S1 and S2 (Supporting Information). **Figure 2a,b** reveals that the

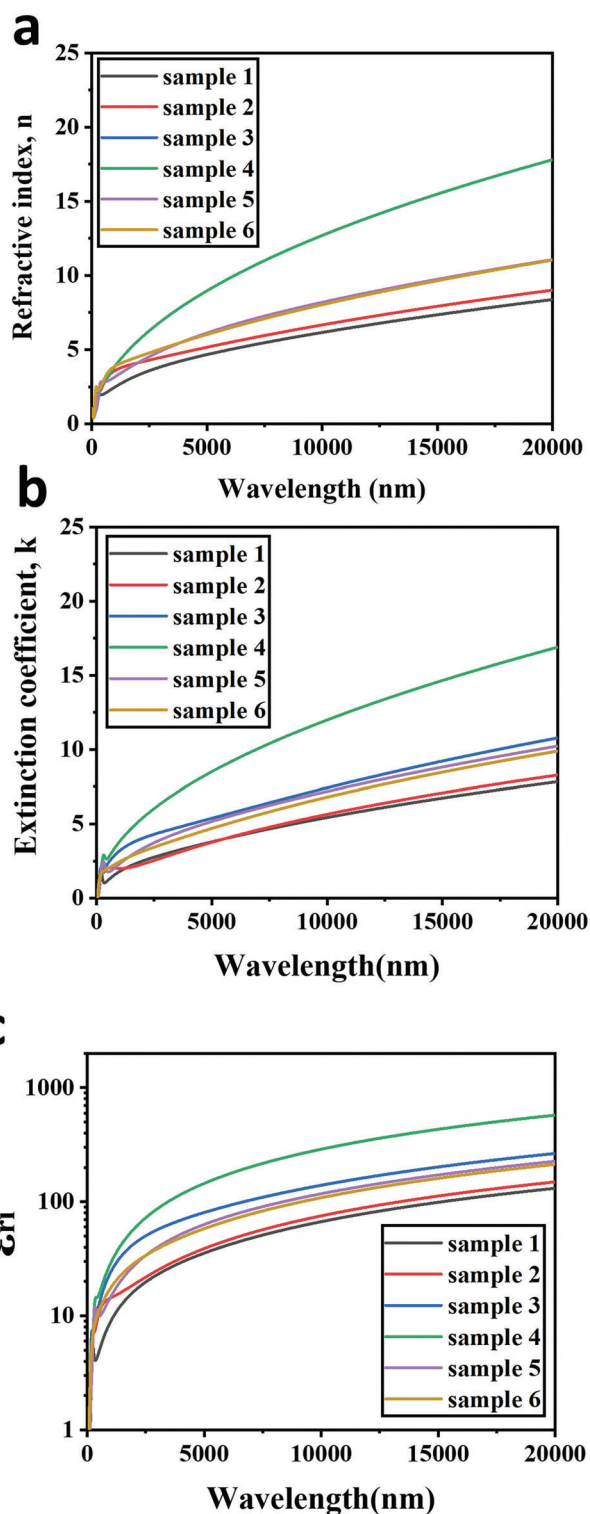


Figure 2. a) Refractive indices and b) extinction coefficients of thin-film metallic glass samples. c) Imaginary part of the dielectric constants of the samples, determined for IR wavelengths from 2.5 to 20 μm .

Table 1. Experimental processing conditions and optical properties of samples of thin-film metallic glass.

Sample	Process pressure [Pa]	DC Power [W]	ω_p^2/γ	Sputtering time [min]
1	0.17	80	7.93	6
2	0.17	90	8.39	6
3	0.17	250	14.94	6
3(C)	0.17	250	74.64	6
4	0.35	250	35.46	6
5	0.31	80	13.96	6
6	0.15	250	13.37	6

optical constants of the samples all increased upon increasing the wavelength. The imaginary part of the dielectric constants of the samples also increased upon increasing the wavelength (Figure 2c). Figure S3 (Supporting Information) provides the optical constants of nickel (Ni) and niobium (Nb). When analyzing the optical parameters of metallic glass samples we found a relationship between the optical parameters and the material properties. Although the optical constants of the different samples were similar, the plasma frequency (ω_p) and damping constant (γ) varied depending on the deposition processes.

We calculated the dielectric constants ($\epsilon_r(\omega)$) of all of the metallic glass samples, where $\epsilon_{re}(\omega)$ and $\epsilon_{ri}(\omega)$ represent the real and imaginary parts, respectively, of the dielectric constant. We obtained the optical parameters through simplification, as demonstrated in Equations (4, 5, and 6):

$$\epsilon_r(\omega) = \epsilon(\infty) - \frac{\omega_p^2}{(\omega^2 + i\gamma\omega)} = \epsilon(\infty) - \frac{\omega_p^2}{\omega^2 + \gamma^2} + i \frac{\omega_p^2\gamma}{\omega(\omega^2 + \gamma^2)} \quad (4)$$

$$\therefore \epsilon_{re}(\omega) = \epsilon(\infty) - \frac{\omega_p^2}{\omega^2 + \gamma^2} \quad (5)$$

$$\epsilon_{ri}(\omega) = \frac{\omega_p^2\gamma}{\omega(\omega^2 + \gamma^2)} \quad (6)$$

where ω_p is the plasma frequency; γ is the damping constant; and ω is the angular frequency. We found, however, that if we examined the IR region using Equation (6), all of our samples were consistent in terms of $\omega < \gamma$ and $\omega < \omega_p$. Simplifying the formula provided $\epsilon_{ri}(\omega)$ and the correlation $\epsilon_{ri}(\omega) \propto \omega_p^2/\omega\gamma$. The value of ω_p^2/γ of the sample could be adjusted by varying the processing conditions, as demonstrated in Figure 3a. To be more explicit about the physical meaning of the optical parameters fitted for each sample, we took the optical conductivity or frequency-dependent conductivity $\sigma(\omega)$ into account and compared it with the values of ω_p and γ using Equation (7), the derivation of which is provided in Figure S5 (Supporting Information). Because we were examining our samples in the IR region where $\omega < \omega_p$ and $\gamma < \omega_p$, we could simplify the real and imaginary parts of Equation (7).

$$\sigma_r(\omega) = \epsilon_0 \left(\frac{\omega_p^2\gamma}{\gamma^2 + \omega^2} \right) \quad \sigma_i(\omega) = \epsilon_0 \left(\frac{\omega_p^2\omega}{\gamma^2 + \omega^2} \right) \quad (7)$$

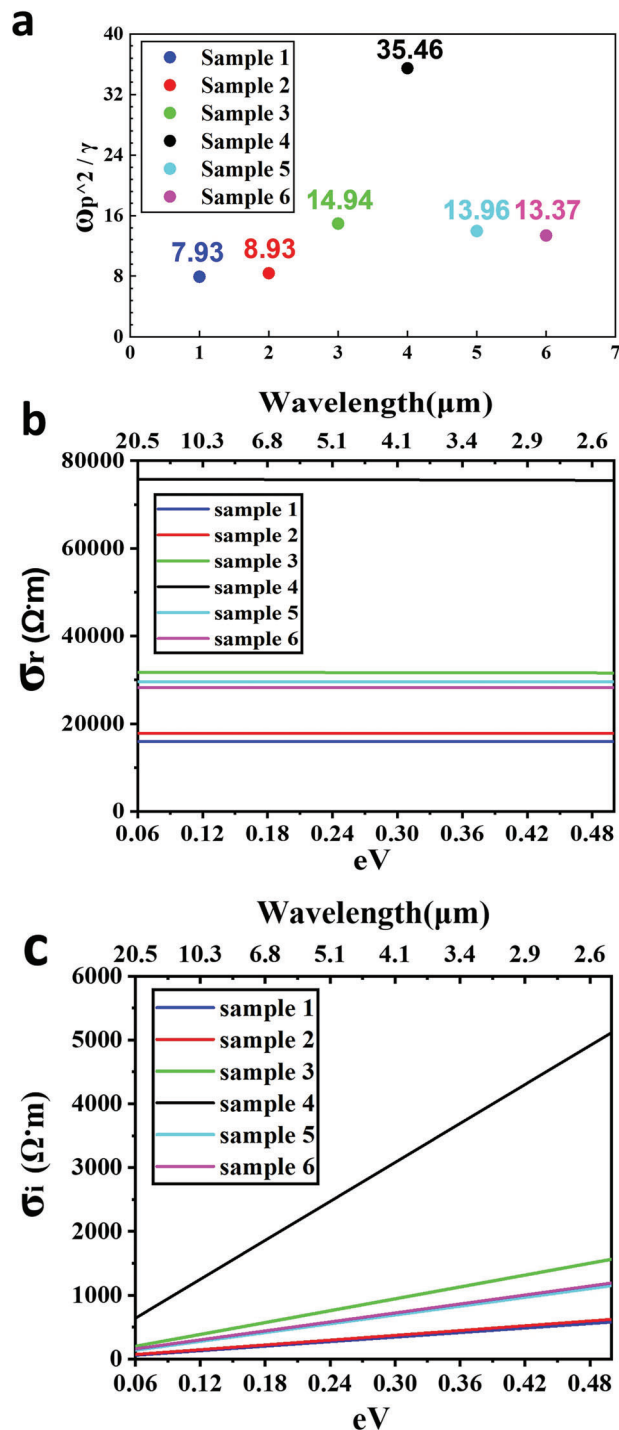


Figure 3. a) Values of ω_p^2/γ and b) real and c) imaginary parts of the optical conductivities of samples of thin-film metallic glass.

$$\sigma_r(\omega) \propto \frac{\omega_p^2}{\gamma^2} \quad (8)$$

$$\sigma_i(\omega) \propto \frac{\omega_p^2\omega}{\gamma^2} \quad (9)$$

Table 2. Plasma frequency, damping constant, and optical conductivities of samples of thin-film metallic glass and Ni and Nb metals.

Sample	ω_p [eV]	γ [eV]	σ_r at 0.5 eV [$\Omega^{-1} \text{ m}^{-1}$]	σ_i at 0.1 eV [$\Omega^{-1} \text{ m}^{-1}$]
1	10.28	14.06	1.607×10^4	1.608×10^4
1(T)	13.40	2.53	1.462×10^5	1.516×10^5
2	11.00	14.42	1.794×10^4	1.796×10^4
3	12.33	10.17	3.191×10^4	3.199×10^4
3(C)	12.43	2.07	1.510×10^5	1.593×10^5
4	16.21	7.41	7.555×10^4	7.588×10^4
5	13.39	12.84	2.984×10^4	2.988×10^4
6	12.80	12.25	2.857×10^4	2.862×10^4
Ni	7.70	0.59	1.252×10^5	2.090×10^4
Nb	19.56	0.94	6.889×10^4	8.612×10^5

Figure 3b,c reveals that the real part of $\sigma(\omega)$ had no correlation with ω . Because ω was much smaller than γ , the equation for $\sigma_r(\omega)$ could be simplified as Equation (8). Thus, the value of $\sigma_r(\omega)$ remained constant upon increasing the value of ω (Figure 3b). The imaginary part of $\sigma(\omega)$ displayed a different trend from that of the real part. When ω increased, the imaginary part also increased because ω was much smaller than γ , leading to the imaginary part of $\sigma(\omega)$ in Equation (7) being simplified as Equation (9). Hence, the value of $\sigma_i(\omega)$ will be proportional to the value of ω , as displayed in Figure 3c. For example, Sample 4 had the highest value of ω_p^2/γ in Figure 3a. Therefore, using Equation (8), we know that the value of $\sigma_r(\omega)$ was the highest, and it remained unchanged upon changing the value of ω . Furthermore, Sample 4 had the lowest value of γ among these samples; therefore, it had the highest value of ω_p^2/γ^2 , leading to the slope of $\sigma_i(\omega)$ in Figure 3c being the largest. As a result, as long as we could obtain the values of ω_p and γ of the samples through optical fitting, we could determine the trends in the values of $\sigma_r(\omega)$ and $\sigma_i(\omega)$ in the thermal IR region. Therefore, as displayed in Figure 3b,c, we would determine that when the value of ω_p^2/γ value of the sample was large, the value of $\sigma(\omega)$ would also be high. Moreover, we found that the value of ω_p^2/γ of the amorphous metallic glass was much smaller than that of the crystalline metal. **Table 2** lists the parameters of the samples.

2.3. Relationship between the Deposition Parameters and the Optical Property of NiNb Metallic Glass

To examine the relationship between the processing conditions and the optical properties of the samples, we investigated the effects of the sputtering power and the processing pressure. Upon increasing the sputtering power, the value of ω_p^2/γ also increased. We suspected that the film became denser upon increasing the sputtering power. Therefore, the atomic arrangement within the film might have featured short-range order, resulting in increased optical conductivity. For Samples 1–3, keeping the processing pressure constant and increasing the sputtering power caused the values of ω_p^2/γ and the optical conductivities increase, with the optical properties of the metallic glass films becoming closer to those of the crystalline metals.

On the other hand, under the same sputtering power, increasing the processing pressure by increasing the Ar flow increased the number of Ar ions. Argon ions with higher energy would result in greater bombardment of the target and more digging of target atoms. When the metallic glass clusters reached the surface of the sample, there would be sufficient energy for migration, such that the atoms could be arranged in short-range order. The moving electrons would be less hindered in the drift process under an electric field with a frequency ω of IR light. We found that the values of $\sigma(\omega)$ and ω_p^2/γ increased for the metallic glass films deposited at a higher Ar flow rate.

In addition, we examined the optical properties of the metallic glass films that had been subjected to long periods of sputtering. Here, we deposited metallic glass films at the same sputtering power and pressure but with different sputtering times. As displayed in **Figure 4a**, Sample 1(T) was deposited for 100 min; the refractive index of Sample 1(T) was slightly smaller than the extinction coefficient k . Both the refractive index and extinction coefficient of Sample 1(T) were significantly larger than those of Sample 1. Moreover, the value of ω_p^2/γ increased from 7.93 for Sample 1 to 70.98 for Sample 1(T) (**Table 3**). To explain this behavior, we speculate that some micro-nanocrystals had formed in the samples after long-term sputtering.

To determine the nanocrystalline phases in the metallic glass samples, we used grazing-incidence X-ray diffraction (GIXRD) and TEM to measure the crystallinities of the metallic glass films. We compared the GIXRD data for Sample 1 with those of the samples prepared with different sputtering times. Figure 4b reveals that the GIXRD intensity of Sample 1(T) was stronger than that of Sample 1, although both samples remained amorphous, as evidenced by their broad peaks. From this GIXRD result, we speculate that a slightly ordered structure had formed during the long-term sputtering process, such that the fitted optical parameters would be close to those of the metals. Figure S4 (Supporting Information) presents the GIXRD data measured for the other samples. Because GIXRD could not provide information about the crystalline structure of the films on the nanoscale, we used TEM to examine the short-range arrangement in Sample 1(T). Figure 4c,d displays the HRTEM images of Sample 1(T). While the specimen was primarily amorphous, some areas featured local atomic short-range ordering. The fast Fourier transform (FFT) pattern taken from the red region in Figure 4c reveals the local atomic arrangement, with the bright spots on the halo indicating the presence of nanocrystals.

Furthermore, we heated Sample 3 and investigated the optical properties of the resulting Sample 3(C). The XRD pattern (**Figure 5a**) revealed that Sample 3 changed from an amorphous state to a crystalline state after being annealed at 900 °C for 1 h. After fitting the optical parameters of Samples 3 and 3(C), we found that the plasma frequency remained almost unchanged after crystallization, but the damping constant had decreased significantly (from 12.43 to 2.07 eV). This behavior indicated that the electrons could migrate freely, because an orderly crystalline arrangement had formed in the structure. Figure 5b reveals that the refractive index of Sample 3(C) was slightly smaller than its extinction coefficient, but both were significantly larger than those of Sample 3. In addition, **Table 1** reveals that the value of ω_p^2/γ value of Sample 3(C) was much larger than that of Sample 3.

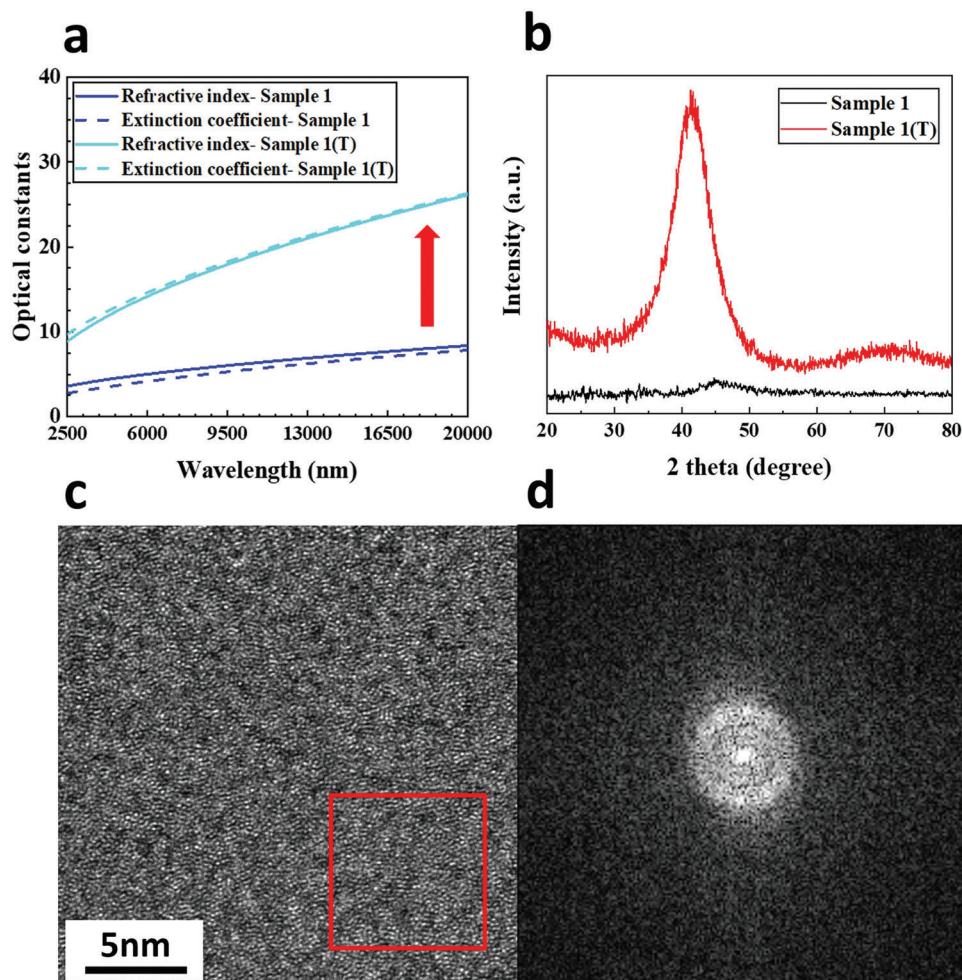


Figure 4. a) Optical constants and b) GIXRD patterns of Samples 1 and 1(T). c) HRTEM image of Sample 1(T). d) Corresponding FFT pattern taken from the red-boxed region in (c).

We also measured the emissivity of the two samples. Because of the crystallization of Sample 3(C), its emissivity decreased significantly in the thermal IR region (Figure 5c).

2.4. Thermal radiation properties of NiNb metallic glass films

After determining the optical properties of the thin-film NiNb samples, we suspected that thin films of metallic glass would have great potential in indoor heat dissipation systems, owing to their emissivity being high when compared with those of crystalline metals. Therefore, we performed optical simulations to determine the highest emissivity possible for metallic glass thin films deposited on a Si substrate. As an illustrative example,

Table 3. Plasma frequency, damping constant, elemental composition, and values of ω_p^2/γ of Samples 1 and 1(T).

Sample	ω_p [eV]	γ [eV]	Ni [at%]	Nb [at%]	ω_p^2/γ	Sputtering time [min]
1	10.28	14.06	53.24	46.66	7.93	6
1(T)	13.40	2.53	48.53	51.46	70.98	100

Figure 6a presents the simulated emissivity of Sample 2 with thicknesses ranging from 5 to 120 nm. The simulation suggested that a broadband emissivity of $\approx 40\%$ could be achieved in the thermal IR region when the thickness of Sample 2 was in the range from 30 to 60 nm. The comparatively higher emissivity at wavelengths of 9 and 13.5 μm corresponds to the intrinsic absorptions of the Si substrate.

Having identified the optimal thickness window to obtain the highest emissivity, we used different sputtering processes to deposit metallic glass thin films onto a Si substrate at thicknesses of ≈ 53 nm (Samples 2 and 6, respectively). We then measured the emissivity of the Si substrate and the metallic glass thin films on the Si substrate. We also compared the emissivity of an Al film coated on a Si substrate (Figure 6b). The average emissivity at wavelengths from 4.5 to 15 μm for the Si substrate was 16.06%. For the thin-film metallic glass Sample 2 on a Si substrate, however, the average emissivity increased dramatically to 44.46%. The measured emissivity was consistent with the simulation data.

Moreover, for the thin-film metallic glass Sample 6 deposited on a Si substrate, the average emissivity was 40.12%. The slightly lower emissivity for Sample 6, relative to Sample 2, arose because

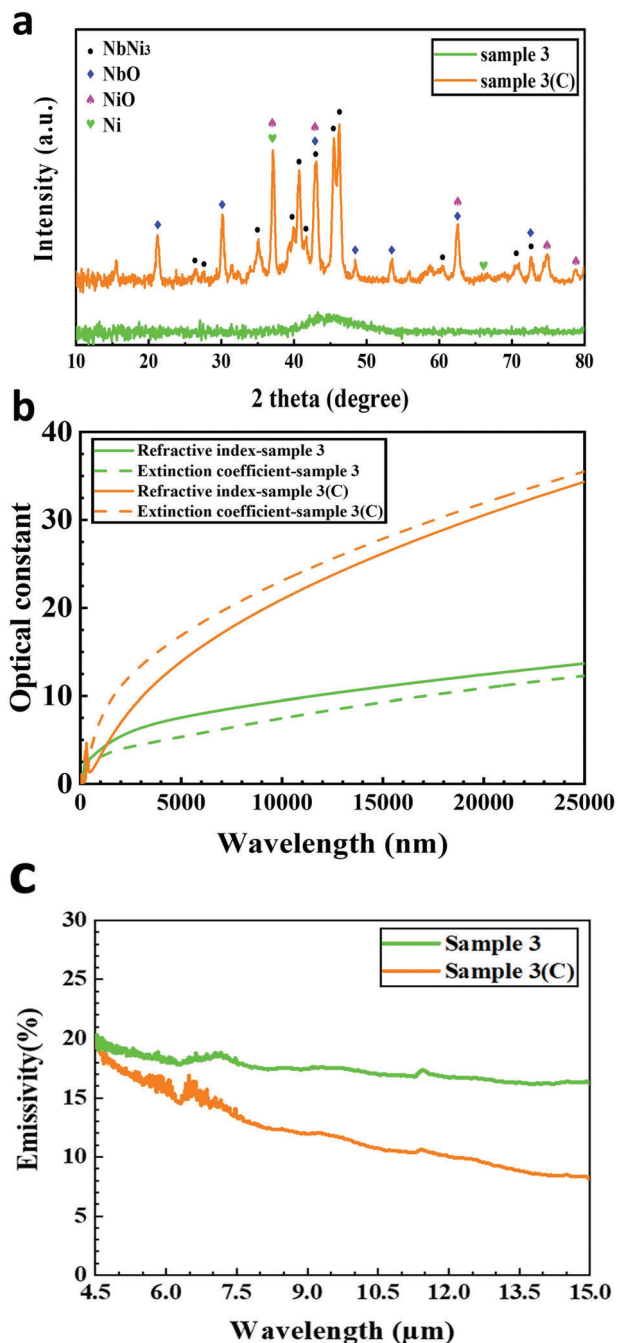


Figure 5. a) GIXRD profiles, b) optical constants, and c) emissivity spectra of Samples 3 and 3(C).

the thickness of the film (53 nm) did not lie in the optimized thickness range (from 20 to 40 nm). On the other hand, the average emissivity of the Al film coated on the Si substrate was only 1.3%, significantly lower than that of thin-film metallic glass samples. Thus, the thermal radiation properties of the thin-film metallic glasses were extraordinary when compared with those of the crystalline metals.

To demonstrate the heat dissipation ability of a thin-film metallic glass, we calculated the radiative cooling power based on the

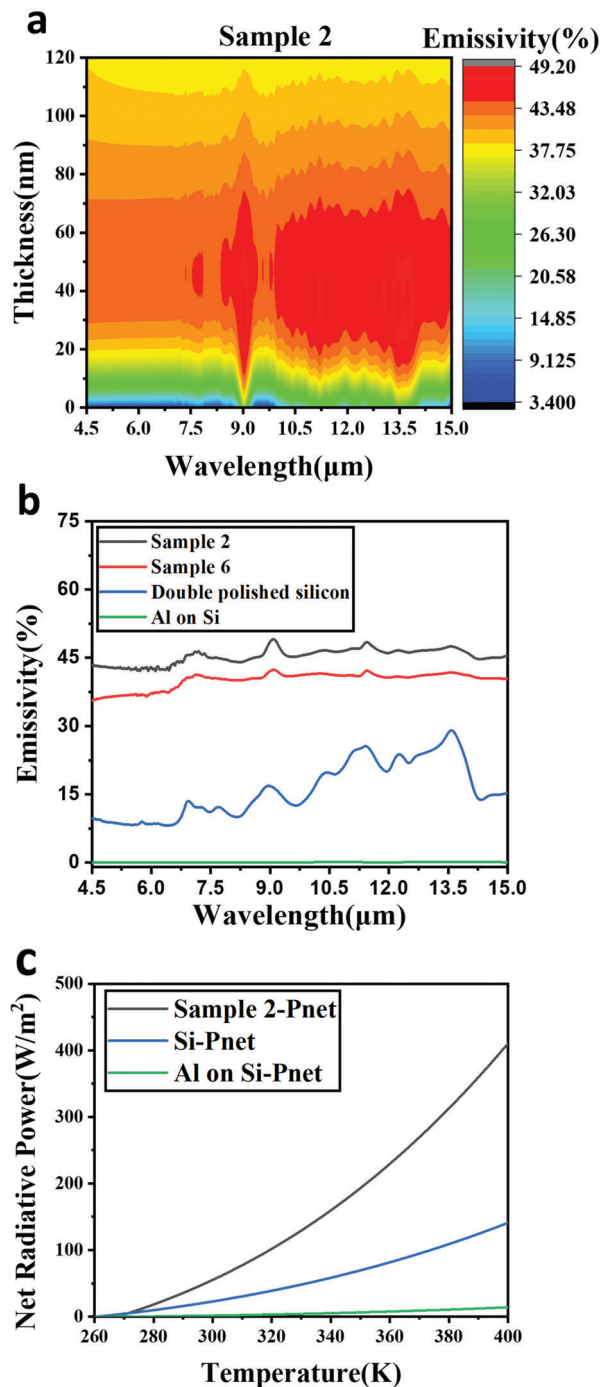


Figure 6. a) Calculated emissivity spectra of Samples 2 prepared with various thicknesses. b) Emissivity spectra of Sample 2 and 6, a 53 nm thick film of Al on a Si substrate, and a bare Si substrate. c) Net radiative power of Sample 2, a Si substrate, and a 53 nm thick film of Al on a Si substrate, measured at various temperatures.

optical spectrum in the thermal IR region. Because we were considering the thermal radiation properties of metallic glass films in indoor conditions (e.g., in semiconductor packaging), we could neglect the radiation of direct sunlight absorption. In addition, we concentrated only on the radiative heat transfer of the metallic

glass film. Therefore, the net radiative power could be simplified, as follows:

$$P_{\text{net}}(T) = P_{\text{rad}}(T) - P_{\text{atm}}(T_{\text{amb}}) \quad (10)$$

where $P_{\text{rad}}(T)$ is the power radiated out from the metallic glass film at a specific temperature and $P_{\text{atm}}(T_{\text{amb}})$ is the power absorbed by the metallic glass film from atmospheric radiation at the temperature of the surroundings.

Figure 6c presents the calculated values of the net radiative power for Sample 2, a Si substrate, and an Al film deposited on a Si substrate, determined at various temperatures. Because of the high emissivity of thin-film metallic glass, the radiative capability of Sample 2 was outstanding relative to that of the Si substrate. The net radiative power of Sample 2 at 373 K reached 282.12 W m^{-2} , whereas the net radiative power of the Si substrate was only 98.89 W m^{-2} . Furthermore, at 373 K, the radiative power of the Al film deposited on the Si substrate was only 9.48 W m^{-2} , due to the low emissivity of the metal. Moreover, the net radiative power increased upon increasing the temperature. The radiative power reached 410.48 W m^{-2} when the temperature was 400 K, nearly threefold the value for the Si substrate. Therefore, our findings reveal that thin-film metallic glasses can display extremely high radiative ability, making them competitive materials for applications requiring the dissipation of heat.

3. Conclusion

The amorphous structure of a thin-film metallic glass increased the opportunity for collisions between the electrons and atoms, thereby increasing the absorption of IR radiation. Accordingly, the emissivity of metallic glass films is generally higher than that of crystalline metals. From an analysis of the relationship between the optical parameters and the material properties, we found that increasing the sputtering power, or performing sputtering at a higher Ar flow rate, led to a sample with a larger value of ω_p^2/γ value of the sample, implying an increase in optical conductivity. Furthermore, with these processing conditions, the optical properties of metallic glass films became closer to those of the crystalline metals. HRTEM revealed the local atomic arrangement in some thin-film metallic glass samples. Finally, optical simulations, performed using optical thin film theory, allowed us to elevate the broadband emissivity experimentally, by suggesting the deposition of a 53 nm thick film of metallic glass on a Si substrate. This thin-film metallic glass enhanced the full-band emissivity at IR wavelengths from 4.5 to 15 μm , with the average emissivity increasing from 16.06% for the Si substrate to 45.35% for the thin-film sample. Furthermore, comparing the thin-film metallic glass to an Al film on a Si substrate, the average emissivity increased from 1.30% to 45.35%. Demonstrating the cooling ability of metallic glass films, we found that Sample 2 coated with metallic glass exhibited a better cooling ability (282.13 W m^{-2}) than a Si substrate at 373 K. We believe that the application of metallic glasses has the potential to overcome the issue of chip heat dissipation. Because metallic glass films have excellent mechanical and chemical properties, their thermal radiation properties could be applied to improve the performance of electronic and optoelectronic devices and systems.

4. Experimental Section

Sample Preparation: The metallic thin film was deposited using DC magnetron sputtering. The chamber was pumped to 0.8 Pa, and then a turbo pump was applied to give high vacuum conditions (4×10^{-4} Pa). The processing pressure for thin-film deposition was controlled by varying the Ar flow rate. The $\text{Ni}_{50}\text{Nb}_{50}$ alloy target was purchased from Gredmann; the substrates for deposition were B270 glass and a double-polished p-type Si (100) wafer. The wafer resistance was 15–25 Ω , and the carrier concentration was in the range from 5×10^{13} to $9 \times 10^{14} \text{ m}^{-3}$.

Characterization: The direct-hemispherical reflectance of the thin film was measured using a UV–vis–NIR spectrophotometer (U4150, HITACHI) and an FTIR spectrometer (VERTEX 70, Bruker) with an integrating sphere (A562 Integrating Sphere). The reflectance at variable angles of the thin film was measured using a UV–vis–NIR spectrophotometer and an FTIR spectrometer equipped with a reflection accessory (A513 variable angle reflection accessory). The emissivity of thin film was also measured using an FTIR spectrometer with a black body furnace (Bruker). The crystalline properties of the films were characterized using XRD (Rigaku TTRAX 3) with monochromatic Cu-K α radiation ($\lambda = 0.15406 \text{ nm}$), operated at 50 kV. High-resolution transmission electron microscopy (HRTEM) was performed using an FEI Tecnai G2 F20 microscope equipped with a high-angle annular-dark-field detector (HAADF); the images were recorded at 200 kV.

Simulations: Reflection spectra recorded at various angles of incidence were used to obtain the optical constants of thin-film metallic glass samples, applying optical thin-film theory^[29] and the Drude model. The thicknesses of metallic glass films on Si substrates were also determined through optical thin film theory to optimize the emissivity in the thermal IR region.

Supporting Information

Supporting Information is available from the Wiley Online Library or from the author.

Acknowledgements

C.-C.L., T.-C.H., and W.-H.W. contributed equally to this work. The authors thank the Ministry of Science and Technology, Taiwan, for supporting this study under contracts MOST 109-2221-E-002-104-MY3, 109-2221-E-002-188-MY3, and 108-2622-E-002-029-CC2.

Conflict of Interest

The authors declare no conflict of interest.

Data Availability Statement

The data that support the findings of this study are available from the corresponding author upon reasonable request.

Keywords

damping constant, optical properties, plasma frequency, thermal emissivity, thin-film metallic glass

Received: June 26, 2023
Revised: August 28, 2023
Published online: October 12, 2023

[1] X. Wei, C. Ying, J. Wu, H. Jiang, B. Yan, J. Shen, *Materials* **2019**, *12*, 4147.

- [2] Z. Q. Ren, A. A. Churakova, X. Wang, S. Goel, S. N. Liu, Z. S. You, Y. Liu, S. Lan, D. V. Gunderov, J. T. Wang, R. Z. Valiev, *Mater. Sci. Eng., A* **2021**, *803*, 140485.
- [3] J. J. Si, X. H. Chen, Y. H. Cai, Y. D. Wu, T. Wang, X. H. Hui, *Corros. Sci.* **2016**, *107*, 123.
- [4] L. Jiang, Z. Q. Chen, H. B. Lu, H. B. Ke, Y. Yuan, Y. M. Dong, X. K. Meng, *J. Mater. Sci. Technol.* **2021**, *79*, 88.
- [5] A. I. Salimon, M. F. Ashby, Y. Bréchet, A. L. Greer, *Mater. Sci. Eng., A* **2004**, *375–377*, 385.
- [6] J. Yu, Y. Ding, C. Xu, A. Inoue, T. Sakurai, M. Chen, *Chem. Mater.* **2008**, *20*, 4548.
- [7] P. Yiu, W. Diyatmika, N. Bönninghoff, Y.-C. Lu, B.-Z. Lai, J. P. Chu, *J. Appl. Phys.* **2020**, *127*, 030901.
- [8] Q. P. Cao, Y. Ma, C. Wang, X. D. Wang, J. Z. Jiang, *Thin Solid Films* **2014**, *561*, 60.
- [9] C. Wang, Q. P. Cao, X. D. Wang, D. X. Zhang, S. X. Qu, J. Z. Jiang, *J. Alloys Compd.* **2017**, *696*, 239.
- [10] C. R. Onyeagba, M. Valashani, H. Wang, C. Brown, P. Yarlagadda, T. Tesfamichael, *Surf. Interfaces* **2023**, *40*, 103090.
- [11] P. Yiu, N. Bönninghoff, J. P. Chu, *Surf. Coat. Technol.* **2022**, *442*, 128274.
- [12] T. Stefanov, H. V. R. Maraka, P. Meagher, J. Rice, W. Sillekens, D. J. Browne, *J. Non-Crystalline Solids: X* **2020**, *7*, 100050.
- [13] Y.-C. Lu, W.-H. Chiang, C.-Y. Liu, J. P. Chu, H.-C. Ho, C.-H. Hsueh, *Sens. Actuators, B* **2021**, *329*, 129132.
- [14] Y.-J. Yeh, C.-Y. Liu, J. P. Chu, W.-H. Chiang, K.-L. Tung, *Surf. Coat. Technol.* **2022**, *436*, 128285.
- [15] C. Yang, C. Zhang, L. Liu, *J. Alloys Compd.* **2017**, *728*, 289.
- [16] W. Yao, Q. P. Cao, S. Y. Liu, X. D. Wang, H. J. Fecht, A. Caron, D. X. Zhang, J. Z. Jiang, *Acta Mater.* **2020**, *194*, 13.
- [17] H. Jia, T. Xu, W. Yao, Q. Cao, X. Wang, J. Z. Jiang, D. Zhang, *Nanotechnology* **2021**, *33*, 335702.
- [18] C. Uzun, C. S. Meduri, S. Jagdale, G. Kumar, A. A. Bernussi, *Opt. Mater.: X* **2021**, *12*, 100095.
- [19] J. H. Weaver, C. Krafka, D. W. Lynch, E. E. Koch, *Appl. Opt.* **1981**, *20*, 1124_1.
- [20] V. Pacheco, D. Karlsson, J. J. Marattukalam, M. Stolpe, B. Hjörvarsson, U. Jansson, M. Sahlberg, *J. Alloys Compd.* **2020**, *825*, 101614.
- [21] B. Sarac, Y. P. Ivanov, A. Chuvilin, T. Schöberl, M. Stoica, Z. Zhang, J. Eckert, *Nat. Commun.* **2018**, *9*, 1333.
- [22] J. Hansson, T. M. J. Nilsson, L. Ye, J. Liu, *Int. Mater. Rev.* **2018**, *63*, 22.
- [23] A. L. Moore, L. Shi, *Mater. Today* **2014**, *17*, 163.
- [24] X. Wang, H. Jiang, *Appl. Therm. Eng.* **2018**, *145*, 674.
- [25] F. Ismayilov, A. Akturk, Y. Peles, *Case Stud. Therm. Eng.* **2021**, *26*, 101028.
- [26] D. Hithaish, V. Saravanan, C. K. Umesh, K. N. Seetharamu, *Therm. Sci. Eng. Progress* **2022**, *30*, 101246.
- [27] M. M. Hossain, M. Gu, *Adv. Sci.* **2016**, *3*, 1500360.
- [28] J. B. Pendry, A. J. Holden, W. J. Stewart, I. Youngs, *Phys. Rev. Lett.* **1996**, *76*, 4773.
- [29] W. L. Bade, *J. Chem. Phys.* **1957**, *27*, 1280.